

# Interpreting Temporal Graph Neural Networks with Koopman Theory

Michele Guerra<sup>1</sup>, Simone Scardapane<sup>2</sup>, and Filippo Maria Bianchi<sup>1,3</sup>

<sup>1</sup>UiT The Arctic University of Norway, Department of Mathematics and Statistics, Norway.

<sup>2</sup>Sapienza Università di Roma, Department of Information Engineering, Electronics and Telecommunications, Italy.

<sup>3</sup>NORCE Norwegian Research Centre AS, Norway.

## Abstract

Spatiotemporal graph neural networks (STGNNs) have shown promising results in many domains, from forecasting to epidemiology. However, understanding the dynamics learned by these models and explaining their behaviour is significantly more complex than for models dealing with static data. Inspired by Koopman theory, which allows a simpler description of intricate, nonlinear dynamical systems, we introduce an explainability approach for temporal graphs. We present two methods to interpret the STGNN’s decision process and identify the most relevant spatial and temporal patterns in the input for the task at hand. The first relies on dynamic mode decomposition (DMD), a Koopman-inspired dimensionality reduction method. The second relies on sparse identification of nonlinear dynamics (SINDy), a popular method for discovering governing equations, which we use for the first time as a general tool for explainability. We show how our methods can correctly identify interpretable features such as infection times and infected nodes in the context of dissemination processes.

## 1 Introduction

Many complex phenomena can be described by the dynamics of items interacting with each other in space and time, leading to complex spatiotemporal relationships that are naturally modelled by temporal graphs (TGs) [10]. Examples are roads and junctions in traffic dynamics [39], arms and legs during human motions [17], infections during social contacts [13], social interactions during events [12], brain activity [6], atmospheric events [26], and many more.

Due to their complexity, it is difficult for machine learning models to take advantage of both spatial and temporal patterns. Recently, spatiotemporal graph neural networks (STGNNs) have emerged as powerful baselines in this scenario [23, 30, 8, 7]. As a result, model explainability for STGNNs has become a primary concern in the field [14]. Despite

preliminary works extending standard explainability techniques to STGNNs for some specific applications in the energy and medical fields [37, 36, 6, 1], the presence of both spatial and temporal components combined with the black-box nature of neural networks still makes these models particularly difficult to interpret.

Koopman theory allows to reformulate a complicated nonlinear dynamical system into a simpler linear representation, at the cost of moving to a potentially infinite-dimensional state space. This approach is particularly useful in many real-world scenarios where the explicit equations of the dynamical system are unknown, but many observation data are available. Since deep learning models can be seen as dynamical systems, Koopman theory was recently applied to design interpretable deep learning architectures [24, 25], or to perform post hoc analyses [31]. Additionally, relevant to TGs is the work done in [28, 27], which is however limited to the analysis of metastable states of the human microbiome.

We extend this line of work by introducing a spatiotemporal model that is trained to transform the complex dynamics of the input TG into a linear dynamics of the embeddings while preserving the model’s accuracy and being *interpretable*. Analysing the model’s embeddings with Koopman-inspired techniques, like dynamic mode decomposition (DMD), allows us to recover both the temporal patterns and the subgraphs that are responsible for the model’s decision-making process. Additionally, we propose for the first time to use sparse identification of nonlinear dynamics (SINDy) – a popular algorithm introduced to find governing equations for complex dynamics – as an explainability method for TGs.

We apply our approach on a Graph Convolutional Recurrent Network (GCRN), but our techniques are general and can be applied to any STGNNs. In our experiments, we demonstrate how the proposed methods correctly highlight important features of the input TG. In particular, in the case of dissemination processes, the explanations accurately locate the times an infection occurs and the nodes involved.

## 2 Background

### 2.1 Koopman operator theory

In [19], Koopman proved how to translate a finite-dimensional nonlinear dynamical system into an infinite-dimensional linear one. Consider a discrete<sup>1</sup> dynamical system on a  $D$ -dimensional state space  $\mathcal{M}$

$$\mathbf{x}_{t+1} = F(\mathbf{x}_t), \quad (1)$$

with state  $\mathbf{x} \in \mathcal{M}$  and flow map  $F : \mathcal{M} \rightarrow \mathcal{M}$ . Let  $\varphi : \mathcal{M} \rightarrow \mathbb{C}$  be an *observable* of the Hilbert space  $L^2$ , i.e.  $\varphi$  is measurable and the Lebesgue integral of the square of the absolute value of  $\varphi$  is finite. Then define the (discrete-time) Koopman operator  $\kappa$  as

$$\kappa\varphi(\mathbf{x}_t) = \varphi(F(\mathbf{x}_t)) = \varphi(\mathbf{x}_{t+1}). \quad (2)$$

The Koopman operator acts on the infinite-dimensional space of observables but has the benefit of being linear

$$\begin{aligned} \kappa(a\varphi_1(\mathbf{x}) + b\varphi_2(\mathbf{x})) &= a\varphi_1(F(\mathbf{x})) + b\varphi_2(F(\mathbf{x})) \\ &= a\kappa\varphi_1(\mathbf{x}) + b\kappa\varphi_2(\mathbf{x}). \end{aligned} \quad (3)$$

#### 2.1.1 Dynamic mode decomposition

In some rare cases, it is possible to find a finite-dimensional subspace of  $L^2$ , so the Koopman operator, restricted to that subspace, is both finite-dimensional and linear, allowing the well-studied descriptions of linear systems [29].

Recently, some data-driven approaches, founded on Koopman theory, have increased in popularity [3]. The idea is to approximate  $\kappa$  using trajectories  $\{\mathbf{x}_t\}_{t=1}^T$  collected from real dynamical systems, reinforced using a library of nonlinear functions, and then use the approximated  $\kappa$  to simulate and analyse the system.

One of the first classes of algorithms introduced to approximate  $\kappa$  was dynamic mode decomposition (DMD) [33]. It was introduced in fluid dynamics and transport processes to extract relevant information directly from data, without necessarily knowing the governing equation of the dynamics. The link to the Koopman operator was only clarified later [20, 2].

Suppose we have a dynamical system described by (1), of which we collect some measurements  $\mathbf{h}_t = \varphi(\mathbf{x}_t) \in \mathbb{R}^F$  at regularly spaced times  $t_i$ , then we can build two matrices of snapshots

$$\begin{aligned} \mathbf{H} &= (\mathbf{h}_1, \mathbf{h}_2, \dots, \mathbf{h}_{T-1}) \\ \mathbf{H}' &= (\mathbf{h}_2, \mathbf{h}_3, \dots, \mathbf{h}_T). \end{aligned} \quad (4)$$

Then the matrix  $\mathbf{C} \in \mathbb{R}^{F \times F}$  given by  $\mathbf{H}' \simeq \mathbf{C}\mathbf{H}$ , that is  $\mathbf{C} = \mathbf{H}'\mathbf{H}^\dagger$ ,<sup>2</sup> approximates the Koopman

<sup>1</sup>The description can be extended to the continuous case [29], but our application uses discrete time, so we will focus on the discrete case only.

<sup>2</sup>Where  $\dagger$  is the Moore–Penrose pseudoinverse.

operator [20]. Since the matrix  $\mathbf{C}$  can be large, the DMD algorithm takes first a singular value decomposition (SVD) or principal component analysis (PCA) of the data matrix  $\mathbf{H}$ , before producing a rank-reduced matrix  $\mathbf{C}$  [20]. The projection of states  $\mathbf{h}_t$  on the  $i$ -th eigenvector of  $\mathbf{C}$ ,  $s^{(i)}(t)$ , is called *Koopman mode* and contains useful information about the dynamics.

The original DMD algorithm described above has been further developed to extend its use and applicability to a wider range of contexts, beyond the fluid dynamics case, and to tackle some of its shortcomings. A review of DMD variations can be found in [34, 3]. For implementations in Python, we refer to [11, 15].

#### 2.1.2 Sparse identification of nonlinear dynamics

In the context of discovering and approximating governing equations from data, another approach, alternative to DMD, was introduced under the name sparse identification of nonlinear dynamics (SINDy) in [5]. The idea is to approximate the dynamics in (1) with a library of pre-determined nonlinear functions, only a few of which will be relevant [4].

Consider the following matrices of snapshots of the system's state  $\mathbf{x}_t \in \mathbb{R}^D$

$$\begin{aligned} \mathbf{X} &= (\mathbf{x}_1, \mathbf{x}_2, \dots, \mathbf{x}_{T-1})^\top \in \mathbb{R}^{(T-1) \times D} \\ \mathbf{X}' &= (\mathbf{x}_2, \mathbf{x}_3, \dots, \mathbf{x}_T)^\top \in \mathbb{R}^{(T-1) \times D}, \end{aligned} \quad (5)$$

and a library of  $J$  candidate nonlinear functions

$$\Theta(\mathbf{X}) = (\mathbb{I}, \mathbf{X}^2, \dots, \sin(\mathbf{X}), \dots) \in \mathbb{R}^{(T-1) \times D \times J}, \quad (6)$$

where each function is applied to  $\mathbf{X}$  element-wise. The dynamical system (1) can now be approximated with

$$\mathbf{X}' = \Theta(\mathbf{X})\boldsymbol{\xi}, \quad (7)$$

where  $\boldsymbol{\xi} \in \mathbb{R}^J$  is a sparse vector, obtained via sparse regression, that selects only a few of the most relevant terms of the library  $\Theta$ .

If we write  $\boldsymbol{\xi} = (\xi_1, \dots, \xi_J)^\top$ , then equation (7) becomes

$$x_{t+1,d} = \sum_{j=1}^J \Theta(\mathbf{X})_{t,d,j} \xi_j, \quad (8)$$

where each component  $\xi_j$  expresses the importance of the  $j$ -th nonlinear function in  $\Theta$  for the system's dynamics.

## 2.2 Spatiotemporal models

### 2.2.1 Temporal graph

In the present work, we focus on temporal graphs (TGs), i.e. data that express spatial relations like

graphs in which both node labels and the topology are time-dependent. For a formal treatment of TGs and recent reviews of methods and tasks applied on TGs and time series with dependencies expressed as a graph, we refer to [23, 9, 10].

In this work, we rely on the following definition of TG.

**Definition 2.1** (Discrete time TG). Given a set of nodes  $\mathcal{V}$  and a set of edges  $\mathcal{E}$ , we define a temporal graph as a sequence of graphs

$$\mathcal{G} := \{(\mathcal{V}_t, \mathcal{E}_t)\}_{t=1}^T, \quad (9)$$

with  $\mathcal{V}_t \subseteq \mathcal{V}$  and  $\mathcal{E}_t \subseteq \mathcal{E}$ . Each node  $v \in \mathcal{V}_t$  is equipped with a feature vector  $\mathbf{x}_t^v \in \mathbb{R}^D$ .

To simplify the notation, we will not consider features on edges, and the feature of the  $n$ -th node at time  $t$  will be represented by  $\mathbf{x}_{t,n}$ . The adjacency matrix is

$$(\mathbf{A}_t)_{nm} = \begin{cases} 1 & \text{if } (v_n, v_m) \in \mathcal{E}_t \\ 0 & \text{otherwise} \end{cases}, \quad (10)$$

and it varies with time since edges are not guaranteed to exist at all times. We will denote by  $N_G$  the number of TGs in a dataset.

### 2.2.2 Graph Convolutional Recurrent Network

To process TGs, we use a slightly modified version of GCRN [35], which, according to the taxonomy in [23], is a snapshot-based model, i.e. it uses a Graph Convolution Network (GCN) [18] as static model to produce a node embedding for each time step, then a Recurrent Neural Network (RNN) to process the time-evolution.

The encoder is composed of  $L$  layers of the following Long Short-Term Memory (LSTM) module

$$\begin{aligned} \mathbf{x}_{t,n}^{\text{GCN}} &= \text{GCN}(\{\mathbf{x}_{t,m}\}_{v_m \in \mathcal{N}_t(v_n)}, \mathbf{A}_t) \\ \mathbf{i}_{t,n,\ell} &= \sigma(\mathbf{W}^{xi} \mathbf{x}_{t,n}^{\text{GCN}} + \mathbf{W}^{hi} \mathbf{h}_{t-1,n,\ell}) \\ \mathbf{f}_{t,n,\ell} &= \sigma(\mathbf{W}^{xf} \mathbf{x}_{t,n}^{\text{GCN}} + \mathbf{W}^{hf} \mathbf{h}_{t-1,n,\ell}) \\ \mathbf{g}_{t,n,\ell} &= \tanh(\mathbf{W}^{xg} \mathbf{x}_{t,n}^{\text{GCN}} + \mathbf{W}^{hg} \mathbf{h}_{t-1,n,\ell}) \\ \mathbf{o}_{t,n,\ell} &= \sigma(\mathbf{W}^{xo} \mathbf{x}_{t,n}^{\text{GCN}} + \mathbf{W}^{ho} \mathbf{h}_{t-1,n,\ell}) \\ \mathbf{c}_{t,n,\ell} &= \mathbf{f}_{t,n,\ell} \odot \mathbf{c}_{t-1,n,\ell} + \mathbf{i}_{t,n,\ell} \odot \mathbf{g}_{t,n,\ell} \\ \mathbf{h}_{t,n,\ell} &= \mathbf{o}_{t,n,\ell} \odot \tanh(\mathbf{c}_{t,n,\ell}), \end{aligned} \quad (11)$$

where  $\mathcal{N}_t(v_n)$  represents the neighbourhood of the  $n$ -th node  $v_n$  at time  $t$ .

For node-level tasks, the embedding for the  $n$ -th node is given by  $\mathbf{h}_n \in \mathbb{R}^{FL}$ , obtained by concatenating along the layer dimension the embeddings of the last time step  $\mathbf{h}_{T,n,\ell} \in \mathbb{R}^F$ . On the other hand, the output  $y$  of a graph-level task is given by processing

with an Multi-Layer Perceptron (MLP) the sum of all node embeddings  $\mathbf{h} = \sum_{n=1}^{|\mathcal{V}|} \mathbf{h}_n \in \mathbb{R}^{FL}$ :

$$y = \text{MLP}(\mathbf{h}) \in \mathbb{R}. \quad (12)$$

In the case of a TG binary classification task, the model is trained using a binary cross-entropy term between the model's output  $y$  and the class label  $\hat{y}$

$$\ell_{\text{bce}}(y, \hat{y}) = -(\hat{y} \log \sigma(y) + (1 - \hat{y}) \log(1 - \sigma(y))). \quad (13)$$

## 3 Methods

### 3.1 GCRN with linear dynamics

In general, the sequence of states  $\mathbf{h}_{t,n}$  does not evolve according to the linear dynamics of (2). To overcome this, we introduce an internal state

$$\tilde{\mathbf{h}}_{t+\tau,n,\ell} := \mathbf{K}^\tau \mathbf{h}_{t,n,\ell}, \quad (14)$$

where  $\mathbf{K} \in \mathbb{R}^{F \times F}$  is a trainable parameter that acts as Koopman operator on  $\tilde{\mathbf{h}}_{t,n}$ . Moreover, to train  $\mathbf{K}$ , we add the following terms to the loss:

- a binary cross-entropy term  $\ell_{\text{rec}}$  between the Koopman-reconstructed output  $\tilde{y} = \text{MLP}(\tilde{\mathbf{h}})$  and the class label  $\hat{y}$ ;
- an observable loss  $\ell_{\text{obs}}$ , which is a ridge regression loss term between the TG embedding at time  $t$ ,  $\mathbf{h}_t$ , and the corresponding Koopman-reconstructed embedding  $\tilde{\mathbf{h}}_t$

$$\ell_{\text{obs}}(\mathbf{h}_t, \tilde{\mathbf{h}}_t) = \text{MSE}(\mathbf{h}_t, \tilde{\mathbf{h}}_t) + \ell_2(\mathbf{K}), \quad (15)$$

where  $\ell_2$  is a weight decay regularisation.

These two terms represent regularisation losses that force the model's encoder to represent an observable  $\varphi$  that satisfies the Koopman operator definition (2), as proposed by [22] and by [24] in a deep learning setting.

We note that the sole purpose of  $\mathbf{K}$  and the internal state  $\tilde{\mathbf{h}}_{t,n}$  is to encourage the state  $\mathbf{h}_{t,n}$  to follow  $\tilde{\mathbf{h}}_{t,n}$ , whose dynamics is, by construction, linear. They are not used to produce the output  $y$ , nor are they involved in the explainability methods described below.

The complete loss is then

$$\ell = \ell_{\text{bce}} + \alpha \ell_{\text{rec}} + \beta \ell_{\text{obs}}, \quad (16)$$

where  $\alpha$  and  $\beta$  are hyper-parameters.

The proposed model is depicted in Figure 1. Notice that, even if here we focus on a GCRN, the proposed approach can be extended to other STGNNs.

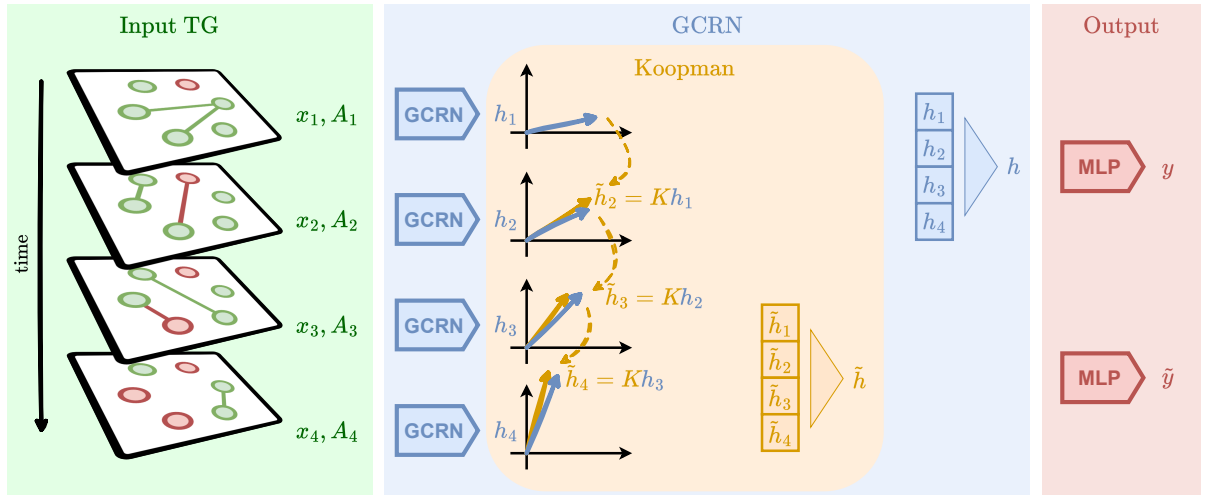


Figure 1: The left-hand side, in green, depicts an example of TG, with node features  $\mathbf{x}_t$  and adjacency matrix  $\mathbf{A}_t$ . In blue, the GCRN processes the input and provides an embedding  $\mathbf{h}_t$  for each time step. The inner yellow box represents the mechanism that encourages the dynamics of embeddings  $\mathbf{h}_t$  to be linear: the loss  $\ell_{\text{obs}}$  in (15) pushes  $\mathbf{h}_{t+1}$  to be a linear transformation of  $\mathbf{h}_t$  (as an example, the picture shows a 2-dimensional rotation). In red, an MLP produces the final output.

### 3.2 Research hypotheses

The task of providing an instance-based explanation is usually declined in computing weights that highlight which parts of the input are more relevant. In the case of TGs, that means finding a weight  $w_t(t)$  for time step  $t$ , and spatial weights  $w_s(n)$  for node  $n$ , or  $w_e(n, m)$  for edge  $(n, m)$ . To properly measure the performance of our explainability methods we require ground truth for each of these quantities. We call  $m_t(t)$  the time ground truth,  $m_s(n)$  the spatial ground truth on nodes, and  $m_e(n, m)$  the spatial ground truth on edges.

Thanks to the proposed regularisation, the model

$$\mathbf{h}_{t+1} = \text{GCRN}(\mathbf{h}_t, \mathbf{x}_t, \mathbf{A}_t). \quad (17)$$

exhibits an approximately linear internal dynamics.<sup>3</sup> On this premise, we introduce two separate post hoc explainability methods – the first based on DMD, the second on SINDy – that provide either temporal or spatial explanations for TGs, or both.

We state here the hypotheses on how DMD and SINDy can explain the GCRN model.

1. The dynamics of at least one DMD mode  $s^{(i)}(t)$  of the TG’s embedding is driven by the input. Hence, the time  $t$  when a significant change happens indicates that something important to the downstream task occurs in the input. Then, we can use the derivative  $ds^{(i)}(t)/dt$  to compute the time weight  $w_t(t)$ .

<sup>3</sup>Refer to Appendix A for a comment on how to extend Koopman to non-autonomous systems.

2. The DMD mode of a node embedding  $s_n^{(i)}(t)$  at each time step (in particular, the last one  $T$ ) identifies whether that node is important for the output or not, and so it is a proxy for the spatial explanation  $w_s(n)$ .
3. SINDy’s regression weights  $\xi_j$  can be used to compute the edge explanation, i.e.  $w_e(n, m)$ .

#### 3.2.1 Explainability using DMD

Thanks to the auxiliary losses in (16), we expect the dynamics of the embeddings of the node  $\mathbf{h}_{t,n}$  and of the whole TG  $\mathbf{h}_t$  to be approximately linear. We can then apply DMD to analyse the trajectories of the GCRN’s states and shed some light on the input and its processing by GCRN.

To reduce the computational complexity of the analysis, a common first step [31] is to apply PCA or SVD to reduce the dimensionality of the embeddings from  $FL$  to  $f$ . Let  $\mathbf{h}'_{t,n} \in \mathbb{R}^f$  and  $\mathbf{h}'_t \in \mathbb{R}^f$  be the embeddings of the nodes and the whole TG, respectively, projected onto the principal components.

To apply DMD on the whole dataset we use ridge regression to fit an operator  $\mathbf{C} \in \mathbb{R}^{f \times f}$  on a training portion of the TGs’ embeddings dataset

$$\mathbf{h}'_{t+1} = \mathbf{C}\mathbf{h}'_t. \quad (18)$$

We can then diagonalise  $\mathbf{C}$ , with eigenvalues  $\lambda_i \in \mathbb{C}$  and eigenvectors  $\mathbf{v}_i \in \mathbb{C}^f$ , and study the dynamics along the eigenspaces  $\langle \mathbf{v}_i \rangle$ . We denote  $s^{(i)}(t) = \mathbf{v}_i^\top \mathbf{h}'_t$  the Koopman mode at time  $t$  on the  $i$ -th eigenspace (ordered according to the magnitude of the corresponding eigenvalue  $\lambda_i$ ). The analysis of

Koopman modes is then performed on the validation set, which allows us to evaluate the generalisation capability of the explainability framework.

On the other hand, to apply DMD on the nodes we focus on a single TG at a time, say  $\mathcal{G}$ , and consider its nodes' embeddings  $\mathbf{h}'_{t,n}$  to fit a matrix  $\mathbf{C}_{\mathcal{G}} \in \mathbb{R}^{f \times f}$

$$\mathbf{h}'_{t+1,n} = \mathbf{C}_{\mathcal{G}} \mathbf{h}'_{t,n}. \quad (19)$$

As in the previous case, we diagonalise  $\mathbf{C}_{\mathcal{G}}$  and compute Koopman modes for nodes,  $s_n^{(i)}(t)$ . Unlike before, however, we cannot split the nodes of the TG  $\mathcal{G}$  in training and validation sets. Thus, we fit and analyse  $\mathbf{C}_{\mathcal{G}}$  on all nodes.

When  $|\lambda_i| < 1$ , we expect both  $s^{(i)}(t)$  and  $s_n^{(i)}(t)$  to decay to 0 and contribute little to the final state (see hypotheses 1 and 2). Meanwhile, when  $|\lambda_i| \simeq 1$ , its dynamics reflect crucial input features, both on its topology and its time dependency, meaning that the  $i$ -th mode explains the model's output. For this reason, we define the time weight directly from the mode derivative as

$$w_{\tau}^{(i)}(t) := \left| \frac{ds^{(i)}(t)}{dt} \right|, \quad (20)$$

and the node weight as a distance from the average

$$w_{\mathbf{s}}^{(i)}(n) := \left| s_n^{(i)}(T) - \frac{1}{|\mathcal{V}|} \sum_m s_m^{(i)}(T) \right|. \quad (21)$$

Hypotheses 1 and 2 can be tested by comparing equations (20) and (21) with  $m_{\tau}(t)$  and  $m_{\mathbf{s}}(n)$ , respectively.

The same approach allows us to define a combined explanation for the whole TG  $\mathcal{G}$  which accounts jointly for both spatial and temporal patterns. Indeed, we can modify definition (21) by considering all times and not just the last one. So we define

$$w_{\mathcal{G}}^{(i)}(t, n) := \left| s_n^{(i)}(t) - \frac{1}{|\mathcal{V}|} \sum_m s_m^{(i)}(t) \right|, \quad (22)$$

such that  $w_{\mathbf{s}}^{(i)}(n) = w_{\mathcal{G}}^{(i)}(T, n)$ . We refer to the Appendix D for a discussion of this approach.

### 3.2.2 Explainability using SINDy

Being a data-driven method to approximate governing equations, also SINDy can learn and store useful information about the dynamics of  $\mathbf{h}'_{t,n}$ . In our case, the matrices defined in equations (5) become

$$\begin{aligned} \mathbf{H}_n &= (\mathbf{h}'_{1,n}, \mathbf{h}'_{2,n}, \dots, \mathbf{h}'_{T-1,n}) \in \mathbb{R}^{T-1, f} \\ \mathbf{H}'_n &= (\mathbf{h}'_{2,n}, \mathbf{h}'_{3,n}, \dots, \mathbf{h}'_{T,n}) \in \mathbb{R}^{T-1, f}, \end{aligned} \quad (23)$$

where  $n = 1, \dots, N$ . The difficult and somewhat arbitrary part of SINDy is the choice of the library

of nonlinearities  $\Theta$ . In our case though, we can take advantage of this flexibility to enforce a bias in the reconstructed dynamics. Due to the GCN layer, each node's state is a nonlinear combination of the neighbouring nodes. Therefore, we can consider as nonlinearities only those terms involving couples of neighbouring nodes

$$\Theta(\mathbf{H}_n) = (\mathbf{H}_n^2, \mathbf{H}_n^3, \mathbf{H}_n \mathbf{H}_{m_1}, \dots, \mathbf{H}_n \mathbf{H}_{m_1}^2, \dots, \mathbf{H}_n \mathbf{H}_{m_2}, \dots, \mathbf{H}_n \mathbf{H}_{m_2}^2, \dots), \quad (24)$$

where all operations are performed element-wise, and node's indices  $m_i$  refer to all those nodes that are connected to the  $n$ -th node at least once, i.e. all those  $m_i$  for which there exists a time  $t$  such that  $(\mathbf{A}_t)_{nm_i} = 1$ . While we could consider higher-order terms such as  $\mathbf{H}_n^2 \mathbf{H}_m^2$  and other nonlinear functions, for the sake of simplicity, we consider up to third-degree monomials.

After introducing an extra index for the node dimension, equation (8) becomes

$$\mathbf{h}'_{t+1,n,d} = \sum_{j=1}^J \Theta(\mathbf{H}_n)_{t,d,j} \xi_{n,j}, \quad (25)$$

where the index  $j = 1, \dots, J$  spans over the monomials of  $\Theta$ , each corresponding by construction to an edge of the input TG. We can then interpret  $\xi_{n,j}$  as a weight that measures how important the edge corresponding to the  $j$ -th monomial is for the dynamics of the  $n$ -th node embedding,  $\mathbf{h}'_n$ . This allows us to construct a weight for each edge  $(n, m)$  as

$$w_{\mathbf{e}}(n, m) := \sum_{n'=1}^N \sum_{j \sim (n,m)} |\xi_{n',j}|. \quad (26)$$

In equation (26), one sum is over all monomials' weights  $\xi_{n',j}$  that refer to the same edge  $(n, m)$ , which expresses how important the edge  $(n, m)$  is for the  $n'$ -th node. The inner sum is needed because different monomials refer to the same edge, e.g. the terms  $\mathbf{H}_n \mathbf{H}_m^2$  and  $\mathbf{H}_n^2 \mathbf{H}_m$  both relate to  $(n, m)$ . The outer sum over all nodes takes into account how important edge  $(n, m)$  is for the whole TG. Once we have a weight for each edge  $w_{\mathbf{e}}(n, m)$ , we can then compare it with the ground truth  $m_{\mathbf{e}}(n, m)$  to test hypothesis 3.

## 4 Experiments

To ensure reproducibility, we open-source our code and experimental setup.<sup>4</sup>

### 4.1 Datasets

The employed datasets consist of TGs whose time-varying topologies describe different types of social

<sup>4</sup>[GitHub repository](#)

interactions. We refer to Appendix B for a description of each dataset. The time-varying node labels  $x_{t,n} \in \{0,1\}$  are produced via a dissemination process simulated with the susceptible-infected model [32]. TGs of class 1 represent a dissemination process. In TGs of class 0 the infected nodes at each time step, originally found via the same dissemination process, are shuffled randomly across the nodes. In each dataset the two classes are balanced. The choice of the employed datasets is motivated by the presence of ground truths for explainability, but the described analyses are general and could be applied to data from different fields.

The time ground truth  $m_t(t)$  provides the number of infections occurring at each time step  $t$  between any two adjacent nodes. That is, a time step  $t$  contributes to  $m_t(t)$  if  $x_{t,n}x_{t,m} = 0$  and  $x_{t+1,n}x_{t+1,m} = 1$  for some adjacent nodes  $n, m$ . The spatial ground truth on nodes  $m_s(n)$  indicates which nodes have been infected:  $m_s(n) = 1$  if node  $n$  has been infected,  $m_s(n) = 0$  otherwise. The spatial ground truth on edges  $m_e(n, m)$  is computed by finding the edges that transmit the infection:  $m_e(n, m) = 1$  if there has been an infection between nodes  $n$  and  $m$ , 0 otherwise.

## 4.2 Metrics

To test hypothesis 1, we measure the correlation between the time ground truth  $m_t(t)$  and the time weight  $w_t^{(i)}(t)$ . Since DMD modes can be quite noisy and  $m_t(t)$  is very sharp, we consider a regularised time ground truth obtained by convolving  $m_t(t)$  with a uniform filter, to make it smoother.

We consider different metrics:

- *F1 with threshold.* F1 score between the time ground truth and those time steps when  $w_t^{(i)}(t) > \delta$ , with  $\delta$  being a threshold.
- *F1 with window average.* As above, but in addition, we first take a running average of  $w_t^{(i)}(t)$  to reduce noise, with window size  $\omega$ .
- *Mann-Whitney U test.* It compares the statistical distribution of  $w_t^{(i)}(t)$  in an interval around the time ground truth values, with the distribution of  $w_t^{(i)}(t)$  in random intervals. We choose the Mann-Whitney U test because it is non-parametric and it doesn't require the two groups to have the same size. We perform this test comprehensively on all the graphs of class 1.

For hypothesis 2, we compare  $w_s^{(i)}(n)$  with the explanation ground truth  $m_s(n)$ . Since finding the explanation is a binary classification problem for each node, we can measure the area under the curve (AUC) score between  $w_s^{(i)}(n)$  and  $m_s(n)$ . Notice that we offered two ways of computing  $w_s^{(i)}(n)$ : one

considering the whole TGs dataset coming from equation (18), and the other by focusing on one input TG at a time from equation (19). In the first case, we call the metric  $AUC_{TG}$ , in the latter we call it  $AUC_{node}$ .

For hypothesis 3, we use weights  $w_e(n, m)$  from equation (26), and compare them with  $m_e(n, m)$  via an AUC score. We call it  $AUC_{edge}^{(2)}$  if the SINDy library  $\Theta$  contains only quadratic terms, and  $AUC_{edge}^{(3)}$  if  $\Theta$  contains cubic terms as well.

## 4.3 Results

Before testing the proposed interpretability tools, we search the GCRN hyperparameters that yield the best classification accuracy. Since the F1 scores depend on the threshold  $\delta$  and the window size  $\omega$ , we perform a grid search on these parameters too. We refer to Appendix C for details. At the bottom of Table 1, which reports results over TGs from class 1, we also report the accuracy of the underlying GCRN model used in our analysis.

**Time explanations** To test hypothesis 1, we report in Table 1 the F1 scores, that compare the time weights  $w_t^{(i)}$  with the time ground truth  $m_t$ , and the Mann-Whitney U test  $p$ -values. For F1 scores we also report a baseline value, computed by considering a naive explainer that outputs  $w_t^{(i)}(t) = 1$  for all  $t$ . As we can see, although the F1 score never reaches, on average, the maximum value of 1, the score is significantly higher than the baseline value for all datasets. In Figure 3 we report two examples of time explanations from the Facebook dataset: on the top, the detection is obtained from thresholding  $w_t^{(i)}(t)$  directly, while in the bottom we first apply the window average on  $w_t^{(i)}(t)$ .

We further verify hypothesis 1 with the Mann-Whitney U test, which shows that the distribution  $f_{gt}$  of  $w_t^{(i)}$  around the ground truth and the distribution  $f_r$  at random times are statistically very

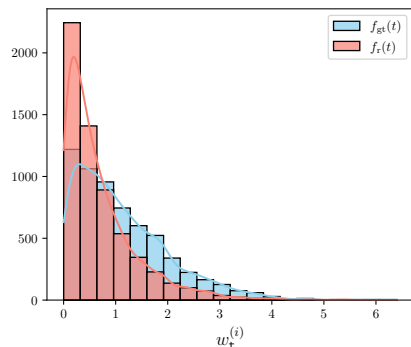
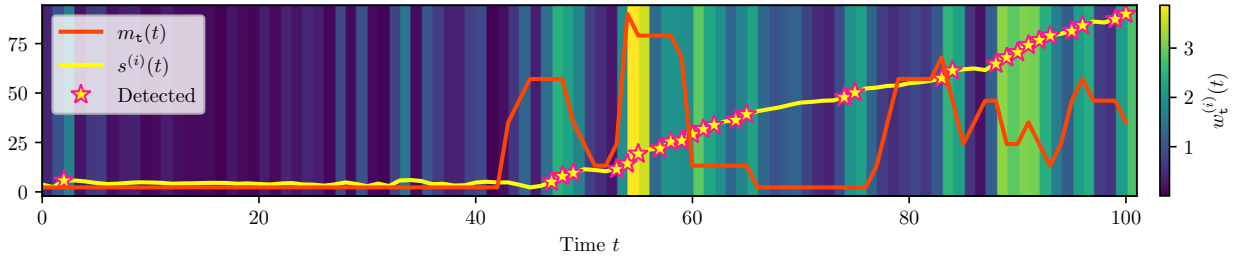


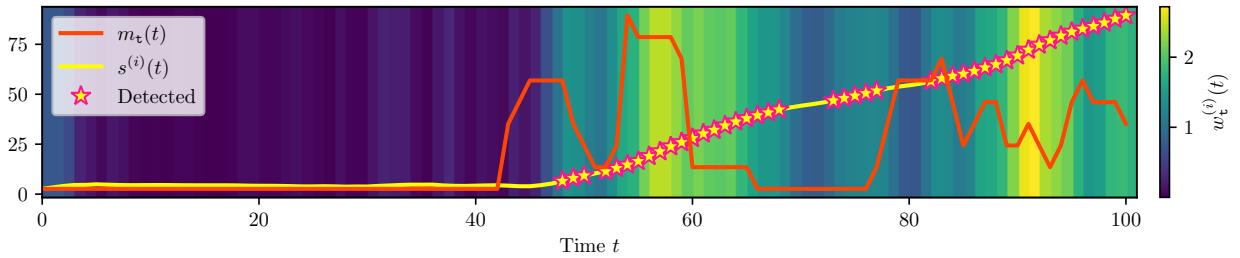
Figure 2: Comparison between the distribution  $f_{gt}$  and the distribution  $f_r$  for the Facebook dataset.

Table 1: Results of experiments.

	Metrics	Facebook	Infectious	DBLP	Highschool	Tumblr
hyp. 1	MW $p$ -value	0.00	0.00	0.00	0.00	0.00
	Threshold (F1)	$0.34 \pm 0.15$	$0.46 \pm 0.12$	$0.31 \pm 0.20$	$0.34 \pm 0.11$	$0.43 \pm 0.15$
	Wind. avg. (F1)	$0.46 \pm 0.22$	$0.43 \pm 0.13$	$0.50 \pm 0.19$	$0.32 \pm 0.13$	$0.50 \pm 0.18$
	F1 baseline	$0.004 \pm 0.014$	$0.03 \pm 0.06$	0	$0.03 \pm 0.04$	$0.01 \pm 0.02$
hyp. 2 & 3	$AUC_{edge}^{(2)}$	$0.60 \pm 0.16$	$0.78 \pm 0.11$	$0.89 \pm 0.10$	$0.76 \pm 0.10$	$0.90 \pm 0.07$
	$AUC_{edge}^{(3)}$	$0.72 \pm 0.14$	$0.88 \pm 0.08$	$0.89 \pm 0.10$	$0.80 \pm 0.09$	$0.87 \pm 0.10$
	$AUC_{TG}$	$0.83 \pm 0.17$	$0.76 \pm 0.14$	$0.73 \pm 0.17$	$0.54 \pm 0.16$	$0.95 \pm 0.04$
	$AUC_{node}$	$0.77 \pm 0.23$	$0.69 \pm 0.16$	$0.76 \pm 0.19$	$0.62 \pm 0.12$	$0.94 \pm 0.08$
	Accuracy	0.98	0.98	1.00	0.94	1.00



(a) Time explanation via threshold. The F1 score is 0.68, affected by some false negatives.



(b) Time explanation via window average. The F1 score is 0.81.

Figure 3: Examples of time explanations for the Facebook dataset. The red line represents the smoothed ground truth  $m_t(t)$ , the yellow line is the relevant Koopman mode  $s^{(i)}(t)$ , the background colour scale shows the explanation weight  $w_t^{(i)}(t)$ , the stars highlight those times  $t$  where  $w_t^{(i)}(t) > \delta$ .

different. As reported in Table 1, the test gives  $p$ -values much smaller than 0.05 for all datasets. Figure 2 shows the two distributions for the Facebook dataset.

**Spatial explanations** To evaluate hypotheses 2 and 3, we report the AUC scores in Table 1. All proposed methods that provide spatial explanations perform consistently well, with some differences between the different datasets. We can notice that  $\text{AUC}_{\text{edge}}^{(3)}$  is almost always larger than  $\text{AUC}_{\text{edge}}^{(2)}$ , as expected, since adding more nonlinearities into the library  $\Theta$  makes SINDy more expressive. In Figure 4, we report an example of an explanation on both nodes and edges.

Despite the analysis presented being instance-based, we can leverage our methods to infer something more general about the behaviour of the trained model. For example, we notice that the weight  $w_{\mathcal{G}}^{(i)}(t, n)$  effectively recognises whether the  $n$ -th node is infected or not at time  $t$ . This means that the quantity  $\sum_n w_{\mathcal{G}}^{(i)}(t, n)$  computed on the whole TG is proportional to the number of infected nodes at each time step  $t$ . In other words, it reveals a behaviour of the GCRN that transcends the specific input, namely that it learns to count infected nodes. Even though this information alone is not sufficient to tell the two classes apart, it is an implicit feature that emerges as the model learns to solve the task at hand. Therefore, we argue that the proposed tools could also interpret the model behaviour besides the input data.

## 5 Conclusion

In this work, we introduce an explainability approach based on Koopman theory for STGNNs. We show that a modified STGNNs can be trained to represent a Koopman observable, allowing a data-driven analysis of the dynamical system implied by the model’s embeddings which makes the model interpretable. Even though the model represents inputs with complicated spatial and temporal relationships, we manage to effectively capture relevant spatial and temporal patterns that can explain the decision process of the GCRN.

**Acknowledgments** The authors gratefully acknowledge NVIDIA Corporation for the donation of two RTX A6000 that were used in this project.

## References

[1] M. Altieri, M. Ceci, and R. Corizzo. Explainable spatio-temporal graph modeling. In *International Conference on Discovery Science*, pages 174–188. Springer, 2023.

[2] H. Arbabi and I. Mezić. Ergodic theory, dynamic mode decomposition, and computation of spectral properties of the koopman operator. *SIAM Journal on Applied Dynamical Systems*, 16(4):2096–2126, 2017.

[3] S. L. Brunton, M. Budišić, E. Kaiser, and J. N. Kutz. Modern koopman theory for dynamical systems. *SIAM Review*, 64(2):229–340, 2022.

[4] S. L. Brunton and J. N. Kutz. *Data-Driven Science and Engineering: Machine Learning, Dynamical Systems, and Control*. Cambridge University Press, 2 edition, 2022.

[5] S. L. Brunton, J. L. Proctor, and J. N. Kutz. Discovering governing equations from data by sparse identification of nonlinear dynamical systems. *Proceedings of the national academy of sciences*, 113(15):3932–3937, 2016.

[6] L. Chen, Y. Yang, A. Yu, S. Guo, K. Ren, Q. Liu, and C. Qiao. An explainable spatio-temporal graph convolutional network for the biomarkers identification of adhd. *Biomedical Signal Processing and Control*, 99:106913, 2025.

[7] A. Cini, D. Mandic, and C. Alippi. Graph-based Time Series Clustering for End-to-End Hierarchical Forecasting. *International Conference on Machine Learning*, 2024.

[8] A. Cini, I. Marisca, F. M. Bianchi, and C. Alippi. Scalable spatiotemporal graph neural networks. In *Proceedings of the AAAI conference on artificial intelligence*, volume 37, pages 7218–7226, 2023.

[9] A. Cini, I. Marisca, D. Zambon, and C. Alippi. Graph deep learning for time series forecasting. *arXiv preprint arXiv:2310.15978*, 2023.

[10] A. Cini, D. Zambon, and C. Alippi. Sparse graph learning from spatiotemporal time series. *Journal of Machine Learning Research*, 24(242):1–36, 2023.

[11] N. Demo, M. Tezzele, and G. Rozza. Pydmd: Python dynamic mode decomposition. *Journal of Open Source Software*, 3(22):530, 2018.

[12] S. Deng, H. Rangwala, and Y. Ning. Learning dynamic context graphs for predicting social events. In *Proceedings of the 25th ACM SIGKDD International Conference on Knowledge Discovery & Data Mining*, pages 1007–1016, 2019.

[13] C. Fritz, E. Dorigatti, and D. Rügamer. Combining graph neural networks and spatio-temporal disease models to improve the prediction of weekly covid-19 cases in germany. *Scientific Reports*, 12(1):3930, 2022.



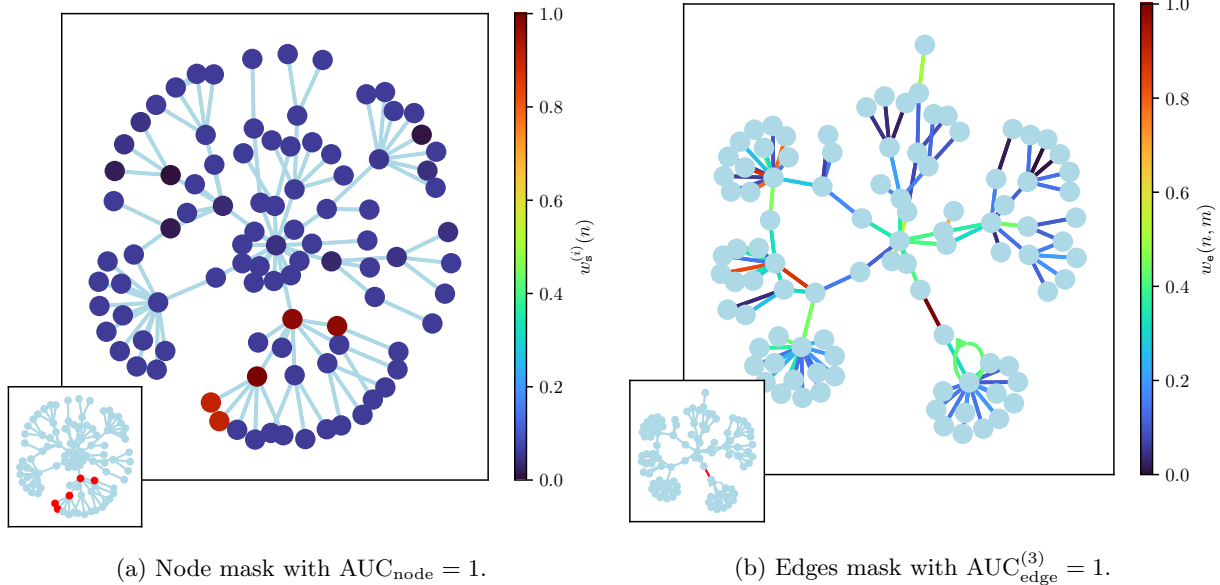


Figure 4: Spatial explanations from Facebook dataset. The colour scale on either nodes or edges represents the explanation weights  $w_s^{(i)}(n)$  (for nodes) and  $w_e(n, m)$  (for edges). The ground truth is reported in the corner.

- [14] V. Hassija, V. Chamola, A. Mahapatra, A. Singal, D. Goel, K. Huang, S. Scardapane, I. Spinelli, M. Mahmud, and A. Hussain. Interpreting black-box models: a review on explainable artificial intelligence. *Cognitive Computation*, 16(1):45–74, 2024.
- [15] S. M. Ichinaga, F. Andreuzzi, N. Demo, M. Tezzele, K. Lapo, G. Rozza, S. L. Brunton, and J. N. Kutz. Pydmd: A python package for robust dynamic mode decomposition. *arXiv preprint arXiv:2402.07463*, 2024.
- [16] L. Isella, J. Stehlé, A. Barrat, C. Cattuto, J.-F. Pinton, and W. Van den Broeck. What’s in a crowd? analysis of face-to-face behavioral networks. *Journal of theoretical biology*, 271(1):166–180, 2011.
- [17] A. Jain, A. R. Zamir, S. Savarese, and A. Saxena. Structural-rnn: Deep learning on spatio-temporal graphs. In *Proceedings of the IEEE conference on computer vision and pattern recognition*, pages 5308–5317, 2016.
- [18] T. N. Kipf and M. Welling. Semi-supervised classification with graph convolutional networks. In *International Conference on Learning Representations*, 2017.
- [19] B. O. Koopman. Hamiltonian systems and transformation in hilbert space. *Proceedings of the National Academy of Sciences*, 17(5):315–318, 1931.
- [20] J. N. Kutz, S. L. Brunton, B. W. Brunton, and J. L. Proctor. *Dynamic mode decomposition: data-driven modeling of complex systems*. SIAM, 2016.
- [21] J. Leskovec, L. Backstrom, and J. Kleinberg. Meme-tracking and the dynamics of the news cycle. In *Proceedings of the 15th ACM SIGKDD international conference on Knowledge discovery and data mining*, pages 497–506, 2009.
- [22] Q. Li, F. Dietrich, E. M. Bollt, and I. G. Kevrekidis. Extended dynamic mode decomposition with dictionary learning: A data-driven adaptive spectral decomposition of the koopman operator. *Chaos: An Interdisciplinary Journal of Nonlinear Science*, 27(10), 2017.
- [23] A. Longa, V. Lachi, G. Santin, M. Bianchini, B. Lepri, P. Lio, F. Scarselli and A. Passerini Graph Neural Networks for Temporal Graphs: State of the Art, Open Challenges, and Opportunities. *Transactions on Machine Learning Research*, 2835-8856, 2023.
- [24] B. Lusch, J. N. Kutz, and S. L. Brunton. Deep learning for universal linear embeddings of nonlinear dynamics. *Nature communications*, 9(1):4950, 2018.
- [25] I. Manojlović, M. Fonoberova, R. Mohr, A. Andrejčuk, Z. Drmač, Y. Kevrekidis, and I. Mezić. Applications of koopman mode analysis to neural networks. *arXiv preprint arXiv:2006.11765*, 2020.

- [26] I. Marisca, C. Alippi, and F. M. Bianchi. Graph-based forecasting with missing data through spatiotemporal downsampling. In *Proceedings of the 41st International Conference on Machine Learning*, volume 235 of *Proceedings of Machine Learning Research*, pages 34846–34865. PMLR, 2024.
- [27] K. Melnyk, S. Klus, G. Montavon, and T. O. Conrad. Graphkke: graph kernel koopman embedding for human microbiome analysis. *Applied Network Science*, 5:1–22, 2020.
- [28] K. Melnyk, K. Weimann, and T. O. Conrad. Understanding microbiome dynamics via interpretable graph representation learning. *Scientific Reports*, 13(1):2058, 2023.
- [29] I. Mezić. Koopman operator, geometry, and learning of dynamical systems. *Not. Am. Math. Soc.*, 68(7):1087–1105, 2021.
- [30] A. Micheli and D. Tortorella. Discrete-time dynamic graph echo state networks. *Neurocomputing*, 496:85–95, 2022.
- [31] I. Naiman and O. Azencot. An operator theoretic approach for analyzing sequence neural networks. In *Proceedings of the AAAI conference on artificial intelligence*, volume 37, pages 9268–9276, 2023.
- [32] L. Oettershagen, N. M. Kriege, C. Morris, and P. Mutzel. *Temporal Graph Kernels for Classifying Dissemination Processes*, pages 496–504. 2020.
- [33] P. J. Schmid. Dynamic mode decomposition of numerical and experimental data. *Journal of fluid mechanics*, 656:5–28, 2010.
- [34] P. J. Schmid. Dynamic mode decomposition and its variants. *Annual Review of Fluid Mechanics*, 54(1):225–254, 2022.
- [35] Y. Seo, M. Defferrard, P. Vandergheynst, and X. Bresson. Structured sequence modeling with graph convolutional recurrent networks. In *Neural Information Processing: 25th International Conference, ICONIP 2018, Siem Reap, Cambodia, December 13-16, 2018, Proceedings, Part I 25*, pages 362–373. Springer, 2018.
- [36] J. Tang, L. Xia, and C. Huang. Explainable spatio-temporal graph neural networks. In *Proceedings of the 32nd ACM International Conference on Information and Knowledge Management*, pages 2432–2441, 2023.
- [37] A. Verdone, S. Scardapane, and M. Panella. Explainable spatio-temporal graph neural networks for multi-site photovoltaic energy production. *Applied Energy*, 353:122151, 2024.
- [38] B. Viswanath, A. Mislove, M. Cha, and K. P. Gummadi. On the evolution of user interaction in facebook. In *Proceedings of the 2nd ACM workshop on Online social networks*, pages 37–42, 2009.
- [39] Q. Zhang, J. Chang, G. Meng, S. Xiang, and C. Pan. Spatio-temporal graph structure learning for traffic forecasting. In *Proceedings of the AAAI conference on artificial intelligence*, volume 34, pages 1177–1185, 2020.

# Supplementary Materials

## A Extension to non-autonomous systems

The dynamical system implied by the GCRN

$$\mathbf{h}_{t+1} = \text{GCRN}(\mathbf{h}_t, \mathbf{x}_t, \mathbf{A}_t) \quad (27)$$

is non-autonomous, unlike the one used in (1). Nonetheless, we can extend its state space to the product space of the original one and the input space, and transform it into an autonomous system

$$\begin{cases} \mathbf{h}_{t+1} = \text{GCRN}(\mathbf{h}_t, \mathbf{x}_t, \mathbf{A}_t) \\ \mathbf{x}_{t+1} = f_x(\mathbf{x}_t, \mathbf{A}_t) \\ \mathbf{A}_{t+1} = f_A(\mathbf{A}_t) \end{cases} . \quad (28)$$

Such a transformation provides the theoretical ground to apply the Koopman theory presented in section 2, even though we only apply our methods to the dynamics of  $\mathbf{h}_t$ .

## B Description of datasets

The datasets employed in the experiments consist of TGs whose time-varying topologies describe different types of social interactions. The *Facebook* dataset is based on the activity of the New Orleans Facebook community over three months [38]; *Infectious* dataset on face-to-face contacts between visitors of the SocioPattern project [16]; *DBLP* dataset on co-author graphs from the DBLP database with the publication year as timestamp; *Highschool* dataset on a contact network from the SocioPattern project of interactions between high school students in twenty seconds intervals over seven days; *Tumblr* dataset on a graph containing quoting between Tumblr users [21]. Table 2 reports the details of each dataset, such as the number of TGs  $N_G$ , the length of the temporal sequence  $T$ , the minimum and maximum number of nodes  $|\mathcal{V}|$  and edges  $|\mathcal{E}|$ .

## C Hyperparameters and implementation details

The presented methods depend on several hyperparameters. Some of these are used to define the architecture and the training of the GCRN employed, others are involved in the explainability methods. Table 3 shows all possible values considered and the optimal hyperparameters configuration used for each dataset. In order to find the best values, we perform a grid search. For those parameters related to the model’s architecture and training, we select the values that yield the highest performance in terms of classification accuracy. For the parameters related to the explainability methods, we use the F1 scores defined in Section 4.2 as the validation metric.

Table 2: Description of datasets.

Dataset	$N_G$	$T$	$ \mathcal{V} $	$ \mathcal{E} $
Facebook	995	106	71-100	176-362
Infectious	200	50	50-50	218-1010
DBLP	755	48	25-99	96-380
Highschool	180	205	26-60	302-1178
Tumblr	373	91	25-99	96-380

The quality of the temporal explanation, used to test hypothesis 1, is measured via F1 score, which depends on a threshold  $\delta$  that highlights those time steps  $t$  such that  $w_{\tau}^{(i)}(t) > \delta$ . As threshold  $\delta$  we either use a fraction of the maximum value of  $w_{\tau}^{(i)}(t)$ , i.e.

$$\delta = \delta' \cdot \max_t w_{\tau}^{(i)}(t), \quad (29)$$

or we consider the distribution of values of  $w_{\tau}^{(i)}(t)$  and use instead

$$\delta = \mu_{w_{\tau}} + \sigma_{w_{\tau}}, \quad (30)$$

where  $\mu_{w_{\tau}}$  and  $\sigma_{w_{\tau}}$  are the time average and standard deviation respectively. In the first case, we report in Table 3 the value of  $\delta'$ , in the second case we write  $\mu_{w_{\tau}} + \sigma_{w_{\tau}}$ .

## D Combined spatiotemporal explanations

As in section 3.2.1, we use the DMD modes to define a spatiotemporal weight

$$w_{\mathcal{G}}^{(i)}(t, n) := \left| s_n^{(i)}(t) - \frac{1}{|\mathcal{V}|} \sum_m s_m^{(i)}(t) \right|, \quad (31)$$

and compare it with a spatiotemporal ground truth  $m_{\text{st}}(t, n)$ .

To assess qualitatively the agreement with the ground truth we refer to Figure 5, which shows an example of a spatiotemporal explanation from the Facebook dataset. The colour scale in the background represents  $w_{\mathcal{G}}^{(i)}(t, n)$  and the red boxes the ground truth  $m_{\text{st}}^{(i)}(t, n)$ .

On the other hand, to provide a more quantitative measure of the agreement between the spatiotemporal explanation  $w_{\mathcal{G}}^{(i)}(t, n)$  and the mask  $m_{\text{st}}(t, n)$ , one option is to rely on the Brier score, defined as

$$\text{BS}(t) := \frac{1}{|\mathcal{V}|} \sum_{n=1}^{|\mathcal{V}|} \left( w_{\mathcal{G}}^{(i)}(t, n) - m_{\text{st}}(t, n) \right)^2. \quad (32)$$

We choose the Brier score to measure accuracy because it correctly accounts for imbalanced classes and it also provides an easily interpretable outcome, where  $\text{BS}(t) = 0$  is the best value and  $\text{BS}(t) = 1$  is the worst. The Brier score is depicted at the bottom of Figure 5: the bumps in the plot correspond to the region with more disagreement between the prediction and the ground truth. In particular, we notice that there is a delay before the explanation realises that a node got infected, and two nodes are false positives, but the Brier score is consistently close to 0.

Table 3: Selected hyperparameters.

	Parameter	Candidates	Facebook	Infectious	DBLP	Highschool	Tumblr
GCRN params.	RNN type	LSTM, GRU	LSTM	LSTM	LSTM	LSTM	LSTM
	$F$	16, 32, 64	64	16	16	16	16
	$L$	1, ..., 10	5	9	5	8	8
	MLP layers	1, ..., 3	1	3	1	1	1
	$\alpha$	1 (fixed)	1	1	1	1	1
	$\beta$	0, 0.05, 0.1, 0.5, 1.0	0.5	0.05	0.05	0.1	0.5
	Batch size	16, 32, 64, 128, 256	16	16	16	32	16
Expl. par.	Dim. red.	PCA, SVD	SVD	PCA	SVD	PCA	SVD
	$f$	10, 16, 32, 64	10	16	16	16	16
	$\delta$	0.4, 0.45, ..., 0.95 or $\mu_{w_{\tau}} + \sigma_{w_{\tau}}$	0.4	0.4	0.4	$\mu_{w_{\tau}} + \sigma_{w_{\tau}}$	0.4
	$\omega$	2, ..., 6	6	6	6	6	6
	Mode $i$	0, 1	0	1	1	0	0

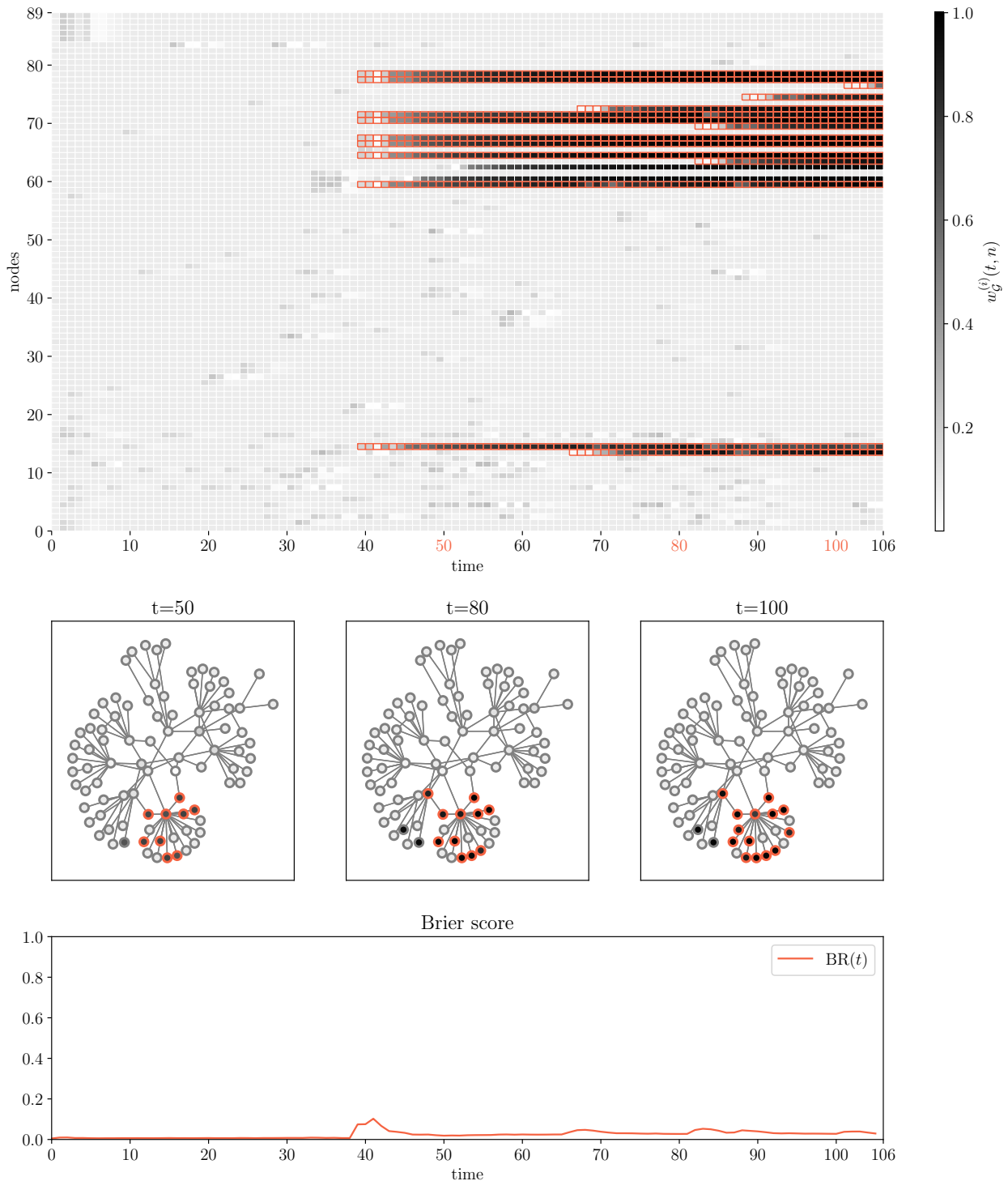


Figure 5: *Top*: The colour scale represents the explanation  $w_G^{(i)}(t, n)$  for each time step ( $x$  axis) and each node ( $y$  axis). The red squares for some values of  $t$  and  $n$  show where  $m_{st}(t, n) = 1$ . *Middle*: They show the TG  $\mathcal{G}$  at three times,  $t = 50, 80, 100$ . Nodes in the ground truth are highlighted in red. *Bottom*: It shows the value of the Brier score  $BS(t)$ .